Nonlinear dynamics of cardiac excitation-contraction coupling: An iterated map study

Zhilin Qu,[1,*] Yohannes Shiferaw,[2] and James N. Weiss[1]
[1]*Cardiovascular Research Laboratory, Department of Medicine (Cardiology), David Geffen School of Medicine, University of California, Los Angeles, California 90095, USA*
[2] *Department of Physics, California State University, Northridge, California 91330, USA*
(Received 4 October 2006; published 30 January 2007)

Cardiac myocytes are excitable cells in which an external current stimulus depolarizes the membrane potential to elicit an action potential. This action potential then triggers calcium release from intracellular stores, which mediates contraction. Conversely, intracellular calcium also modulates membrane currents, affecting action potential morphology and action potential duration (APD). The interactions between action potential and calcium, termed excitation-contraction coupling, give rise to a rich spectrum of nonlinear dynamics, especially at rapid heart rates, which are important for cardiac contraction and the development of lethal arrhythmias. In this study, we developed a nonlinear iterated map model to investigate the dynamics of cardiac excitation-contraction coupling in a periodically stimulated cell. We first studied the nonlinear dynamics due to APD restitution, a functional relation between APD and its preceding diastolic interval. We then studied the nonlinear dynamics due to intracellular calcium cycling when total cell calcium is constant or varies at a beat-to-beat basis. Finally, we studied the nonlinear dynamics due to the bidirectional coupling of the two dynamical systems. Saddle-node bifurcations leading to bistability, period-doubling bifurcations leading to alternans, and period-doubling routes to chaos can independently occur in both action potential or intracellular calcium cycling subsystems as heart rate increases. A Hopf bifurcation leading to quasiperiodicity occurs when the two dynamical systems are coupled. Although these dynamics are predicted from low-dimensional iterated maps, the approach here provides valuable information which can be used as a basis to explore dynamical features of physiologically detailed ionic models, to illuminate experimental findings, and to design experimentally testable predictions for new biological experiments.

DOI: 10.1103/PhysRevE.75.011927 PACS number(s): 87.19.Hh, 87.19.Nn

I. INTRODUCTION

In the normal heart, the cardiac action potential originates in the sinus node and propagates as an electrical wave through the atria, atrioventricular conduction system and the ventricles. In the setting of heart disease, however, heterogeneous electrophysiological properties in different regions of the heart can become large enough to cause wavebreaks inducing reentrant arrhythmias, which may be life threatening due to their rapid rate. Recent evidence indicates that dynamic properties of cardiac excitation-contraction (EC) coupling contribute importantly to functional magnification of tissue heterogeneities promoting arrhythmogenesis [1,2]. At the cellular level, the causes for these dynamics are mainly related to action potential properties, including action potential duration (APD) restitution [3–12], intracellular calcium (Ca) cycling dynamics [13–17], and wave conduction properties such as conduction velocity restitution [11,12,18–20].

The major interactions between the action potential and Ca cycling in cardiac myocytes are illustrated in Fig. 1(A) [21,22]. There are many ion channels in the cell membrane, including sodium (Na), potassium (K), and Ca channels. Na and Ca currents pass inward current while K currents are outward, in accordance with their respective electrochemical driving forces. The action potential is a transient response of the membrane to an external current stimulus, reflecting the competition between fast inward currents and slow outward currents. At rest, the membrane potential of a cardiac myocyte is around −80 mV [see Fig. 1(B)]. External current from the stimulus brings the voltage to a threshold voltage (∼−60 mV) at which the Na channels open. The Na current is an inward current which further depolarizes the membrane potential to above zero. The Na channel inactivates quickly, resulting in a sharp pulselike current. The *L*-type Ca current is another inward current which is activated above −40 mV and inactivates much slower than the Na current, and thus maintains the depolarization phase of the action potential for a longer time. As this current inactivates, the outward K currents increase and eventually exceed the inward currents, repolarizing the membrane back to the resting potential of −80 mV. The Na is pumped out of the cell and the K is pumped back into the cell by the Na-K pump to maintain the resting membrane potential and Na and K homeostasis. Ca homeostasis of the cell is maintained principally by influx through *L*-type Ca channels and extrusion through electrogenic Na-Ca exchange. Ca is also compartmentalized inside the cell, stored in intracellular organelles known as the sarcoplasmic reticulum (SR). Ca entry through the *L*-type Ca channel triggers release of Ca from the SR into the cytoplasm by activating SR Ca release (RyR) channels, through a process called Ca induced Ca release. After Ca is released into the cytoplasm, it is pumped back into the SR by the sarcoplasmic-endoplasmic reticulum Ca ATPase (SERCA) pump, with a small amount of leak from the SR back into the

*Author to whom correspondence should be addressed; Electronic address: zqu@mednet.ucla.edu

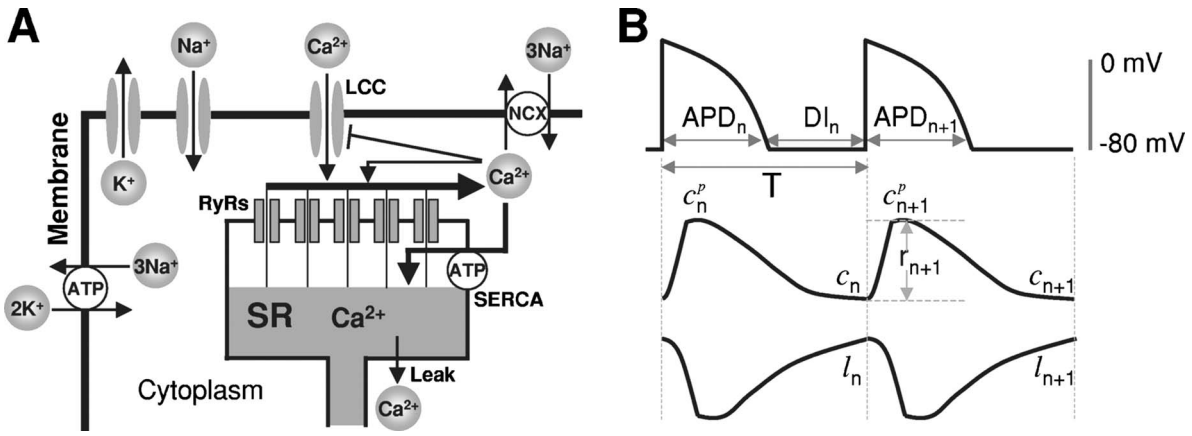

FIG. 1. (A) Schematic illustration of cardiac EC coupling. LCC represents L-type Ca current; NCX represents Na-Ca exchange; SR represents sarcoplasmic reticulum; RyR represents ryanodine receptors (SR Ca release channels); SERCA represents sarcoplasmic-endoplasmic reticulum Ca ATPase (SR Ca uptake pump). See text for details. (B) Graphical definitions of APD, DI, and stimulation period T (upper trace); diastolic Ca (c) at the end of each beat, peak cytoplasmic Ca (c^p), and Ca released (r) from the SR (middle trace); and SR Ca load (l) at the end of each beat (bottom trace), illustrated for the nth and $(n+1)$th beat.

myoplasm. Overall Ca cycling is dominated by the movement between the intracellular compartments, with 70%–90% of the total Ca flux occurring between the SR and cytoplasm, and only 10%–30% across the sarcolemma. Ca cycling is strongly coupled to membrane voltage via Ca sensitive ion channels and transporters. A large Ca release inactivates the L-type Ca current more rapidly, tending to shorten the APD. On the other hand, a large Ca release also promotes Ca efflux via the electrogenic Na-Ca exchange, which generates an inward current which tends to prolong the APD. Depending on which effect dominates, a large Ca release can either shorten or prolong APD. Following previous studies [15,16], we will refer the former effect as *negative* Ca-to-APD coupling, and the latter as *positive* Ca-to-APD coupling. Conversely, a long APD can enhance or diminish Ca release in the subsequent beat, which we refer to as *positive* or *negative* APD-to-Ca coupling, respectively.

Due to the complex nonlinear interactions between membrane potential, ionic currents, and intracellular ion fluxes, a rich spectrum of nonlinear dynamics has been reported at multiple spatial scales, ranging from subcellular to whole cell to multicellular tissue to intact heart [3,18,23–36]. A valuable tool for understanding the mechanisms underlying these dynamics has been low-dimensional iterated maps [3,15,16,24]. Previous studies [15,16] have investigated dynamical instabilities due to EC coupling of isolated cardiac myocytes under periodic stimulations using this approach but have been restricted to general analysis and linear maps. In this study, we have generalized these studies to first develop an EC coupling iterated map model to include most of the up-to-date experimentally observed features with nonlinear maps, which enable more physiologically realistic relationships to be incorporated into the analysis. We then analyze the dynamics of iterated maps for APD and Ca dynamics separately, followed by a detailed analysis of the coupled system.

II. MODEL DEVELOPMENT

In previous studies [3,37], APD has been assumed to be a function of the preceding diastolic interval (DI), which is mainly determined by the kinetics of recovery from inactivation and deactivation of various ion channels. However, as illustrated in Fig. 1(A), since APD is also affected by the Ca transient, here we assume that APD is a function of both the previous DI and the peak cytoplasmic Ca of the present beat, i.e.,

$$a_{n+1} = f(d_n, c^p_{n+1}), \tag{1}$$

where a_{n+1} is the APD of the $(n+1)$th beat, c^p_{n+1} is the peak cytoplasmic Ca of the $(n+1)$th beat, and d_n is the DI of the nth beat, defined as

$$d_n = T - a_n, \tag{2}$$

where T is the period of stimulation. Figure 1(B) shows graphical illustration of the key variables used in this study. The relation between APD and its previous DI, the so-called APD restitution, has been measured in many experimental studies [38–41]. However, the dependence of APD on Ca is variable, such that increased Ca can either shorten or prolong APD depending on experimental conditions [15,16]. For simplicity, we set the function in Eq. (1) into separate voltage-dependent (mainly due to ion channel recovery) and Ca-dependent (mainly due to Ca-dependent ion currents) components as follows:

$$a_{n+1} = f(d_n) + p(c^p_{n+1})a_{n+1}. \tag{3}$$

Since there is no experimental data to show how Ca affects APD, we assume that the magnitude of its effect is proportional to APD of the same [$(n+1)$th] beat, and we simply set $p(c^p_{n+1})$ proportional to the peak cytoplasmic Ca, i.e.,

$$p(c^p_{n+1}) = \gamma c^p_{n+1}, \tag{4}$$

where γ is the parameter describing the coupling strength. $\gamma > 0$ corresponds to positive Ca-to-APD coupling, while $\gamma < 0$ to negative Ca-to-APD coupling. c^p_{n+1} is determined by the following equation [see illustration in Fig. 1(B)]:

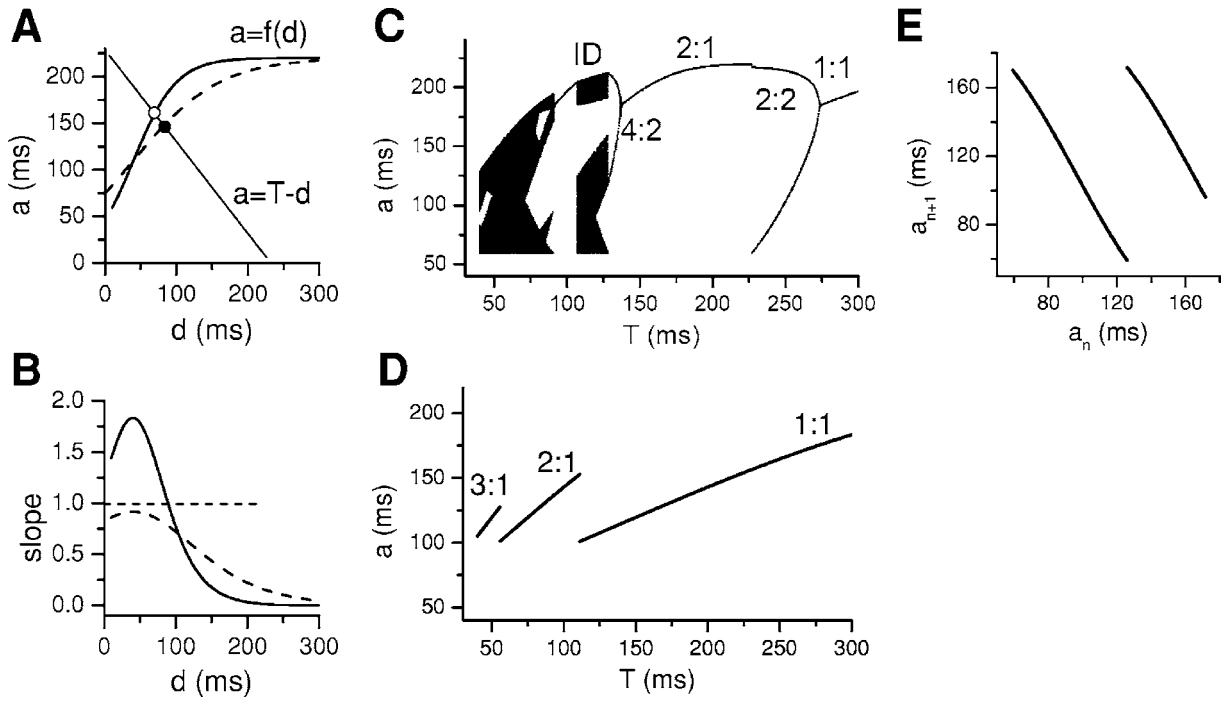

FIG. 2. Dynamics due to monotonic APD restitution curves. (A) Steep and shallow APD restitution curves from Eq. (5) with A_0 =220 ms, A_1=0, d_0=40 ms, τ_0=30 ms (solid line), and τ_0=60 ms (dashed line). The open and filled circles are the steady state solutions for the two APD restitution curves at pacing period T. (B) APD restitution slope for the two APD restitution curves shown in (A). (C) Bifurcation diagram showing APD versus pacing period T for the steeper APD restitution curve in (A), by iterating Eq. (18). The bifurcation sequence is $1:1\rightarrow2:2\rightarrow2:1\rightarrow4:2\rightarrow\mathrm{ID}\rightarrow4:1\rightarrow\mathrm{ID}$, where "$n:m$" indicates that n stimulations cause m different action potentials, which repeat periodically (e.g., "2:2" means that two successive stimuli result in two different APDs, i.e., APD alternans). ID stands for irregular dynamics or dynamic chaos. For each T, we discarded the first 150 APDs and plotted the next 100 APDs. In the alternans (2:2) regime, there are only two APD values although 100 APDs were plotted; however, in the chaotic regime, the values of the 100 APDs are different, resulting in scattered plots. (D) Bifurcation diagram showing APD versus pacing period T for the shallower APD restitution curve in (A), obtained by iterating Eq. (18). (E) a_{n+1} versus a_n in the chaotic regime in C for T=70 ms, showing a discontinuous map similar to the classic shift map.

$$c_{n+1}^{p} = c_n + r_{n+1}, \tag{5}$$

i.e., the peak cytoplasmic Ca is a sum of diastolic cytoplasmic Ca (c_n) and the total Ca released (r_{n+1}) from the SR during the $(n+1)$th beat. c_n is defined as the diastolic Ca in the cytoplasm at the end of the nth beat. The total Ca b_n in the cell at the end of the nth beat is the sum of the diastolic Ca c_n in the cytoplasm and the Ca load l_n in the SR of the nth beat, from which c_n is determined as

$$c_n = b_n - l_n. \tag{6}$$

The equations for b_n, l_n, and r_{n+1} will be shown later. $f(d_n)$ is the APD restitution function, for which we use the following function:

$$f(d_n) = A_0[1 - 1/(1 + e^{(d_n - D_0)/\tau_0})] + A_1 e^{-(d_n - D_1)^2/\tau_1}, \tag{7}$$

where A_0, D_0, τ_0, A_1, D_1, and τ_1 are parameters that control the shape of the APD restitution curve. The rationale for choosing Eq. (7) is as follows. When A_1=0, Eq. (7) is always a monotonically increasing function and saturates at long DIs [see Fig. 2(A) below], similar to most of the experimentally observed APD restitution curves [40,41]. When $A_1 \neq 0$, Eq. (7) can be nonmonotonic or biphasic [see Fig. 3(A) below], which has also been observed in human and animal experiments [39,42].

The total SR Ca load of the present beat (l_{n+1}) is equal to that of the previous beat (l_n) less the Ca released from the SR (r_{n+1}), the Ca leak from the SR (z_{n+1}), and plus the Ca reuptake by the SR (u_{n+1}) of the present beat, i.e.,

$$l_{n+1} = l_n - r_{n+1} - z_{n+1} + u_{n+1}. \tag{8}$$

It has been shown experimentally [43,44] that Ca released from the SR depends on SR Ca load. In addition, the Ca released from the SR is dependent on the magnitude of the L-type Ca current, which is responsible for triggering Ca release from the SR [Fig. 1(A)]. Since the magnitude of the L-type Ca current during an action potential is dependent on the time of recovery from inactivation, the amount of Ca released from the SR is also dependent on the previous DI [45,46]. Furthermore, RyR channels, which open in response to Ca entry from the L-type Ca channel, are believed to be inactive in a Ca-sensitive manner. Hence, on the next beat, the availability of RyR channels to open will be critically dependent on the recovery time duration, i.e., the previous DI. To represent these dependencies mathematically, we de-

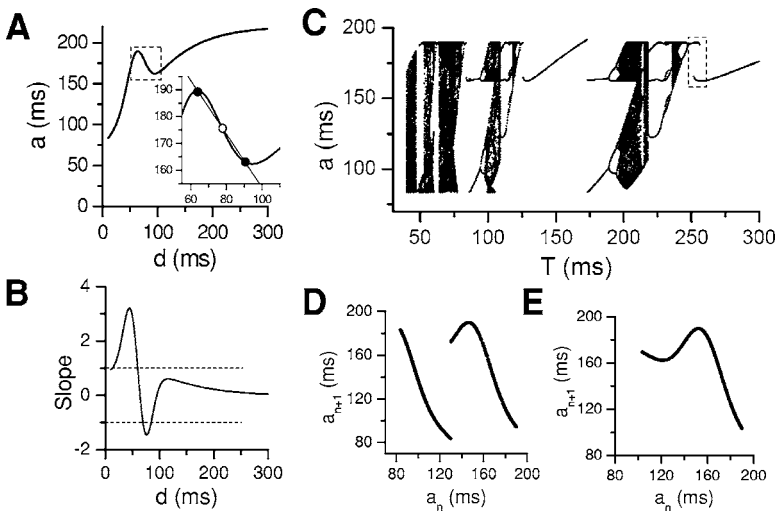

FIG. 3. Dynamics due to a nonmontonic APD restitution curve. (A) APD restitution curve from Eq. (5) with A_0=220 ms, d_0=40 ms, τ_0=60 ms, A_1=60, d_1=60 ms, and τ_1=500 ms. Inset is an amplification of the dashed box showing three steady state solutions (circles) for T=248 ms. (B) APD restitution slope for the APD restitution curve in (A). (C) Bifurcation diagram showing APD versus pacing period T for the APD restitution curve in (A) obtained by iterating Eq. (15). (D) a_{n+1} versus a_n for T=70 ms, showing a discontinuous map. (E) a_{n+1} versus a_n in the chaotic regime in (C) for T=216 ms, showing a unimodal map.

fine the Ca released from the SR as a product of two functions,

$$r_{n+1} = q(d_n)g(l_n) \tag{9}$$

in which $q(d_n)$ describes the restitution properties of SR Ca release, due either to refractoriness of RyR channels or to graded SR Ca release proportional to recovery of the L-type Ca current. Based on the experimental data [45,46], we choose the following restitution function for $q(d_n)$:

$$q(d_n) = (1 - \sigma e^{-d_n/\tau_q}). \tag{10}$$

The release function $g(l_n)$ in Eq. (9) represents the dependence of SR Ca release on the load state of the SR. This functional dependence has been measured, and can be described by a function of the form

$$g(l_n) = l_n[1 - (1 - \alpha)/(1 + e^{(l_n - l_c)/\beta})] \tag{11}$$

which can be fitted directly to experimental data, as will be shown later. α, β, and l_c are parameters that can be determined from fitting the experimental data.

Ca leak from the SR is also a function of SR Ca load [47], i.e.,

$$z_{n+1} = w(l_n), \tag{12}$$

where z_{n+1} denotes the amount of Ca leaked from the SR on the $(n+1)$th beat. Since SR Ca leak is solely a function of SR Ca load, similar to the release function $g(l_n)$, we have not explicitly included it in this study, i.e., the function $g(l_n)$ is taken to represent implicitly the summed effect of SR Ca release and SR Ca leak.

Ca is pumped back into the SR via SERCA pumps, for which we choose the following function:

$$u_{n+1} = u(T)h(c^p_{n+1}), \tag{13}$$

where $u(T)$ reflects the fact that the total Ca pumped into the SR depends on the time duration of pumping [21,48]. This effect can be modeled using

$$u(T) = (1 - \rho e^{-T/\tau_u}). \tag{14}$$

In Eq. (13), $h(c^p_{n+1})$ is the SR Ca uptake function, which, according to experimental data is also a sigmoidal function [49,50]. Here we assume the uptake function to be

$$h(c_p^{n+1}) = \upsilon c^p_{n+1}[1 - 1/(1 + e^{(c^p_{n+1} - c_0)/\theta})], \tag{15}$$

where υ, c_0, and θ are parameters.

The total Ca inside the cell during the $(n+1)$th beat is the total Ca left from the nth beat plus the net Ca influx or efflux during the $(n+1)$th beat, for which we used the following equation:

$$b_{n+1} = b_n - \kappa[c_n - c(T)] + \eta(a_{n+1} - a_n), \tag{16}$$

where η and κ are constants and $c(T)$ is the steady state cytoplasmic Ca at cycle length T, accounting for Ca accumulation in the cell. The second term in Eq. (16) tends to equilibrate the cytoplasmic Ca at $c(T)$. Usually, Ca concentration increases as T decreases [21,41] due to Ca accumulation. Thus, we define $c(T)$ as

$$c(T) = c_0(1 + \varepsilon e^{-T/\tau_c}), \tag{17}$$

where τ_c and ε are constants. Since APD affects the L-type Ca current and the Na-Ca exchange current, affecting Ca flux through the cell membrane and thus the total Ca in the cell, we model this effect by adding the term $\eta(a_{n+1} - a_n)$ into Eq. (16). At the equilibrium state, $a_{n+1} = a_n$, the contribution of this term is zero. But at periodic or chaotic states, $a_{n+1} \neq a_n$, then Ca may enter or exit the cell on a beat-to-beat basis. $\eta > 0$ indicates positive APD-to-Ca coupling, while $\eta < 0$ indicates negative APD-to-Ca coupling.

III. DYNAMICAL INSTABILITIES DUE TO APD RESTITUTION

The effects of the slope of APD restitution on APD dynamics during periodic pacing have been widely studied [3,42,51–53]. Here we outline the dynamics due to APD restitution as a prerequisite for studying the new dynamics due to EC coupling. During periodic pacing with period T, the iterated map based on APD restitution is

$$a_{n+1} = f(d_n) = f(T - a_n). \tag{18}$$

The steady state solution of Eq. (18) can be obtained from the equation $a_s = f(T - a_s)$ if the function f is known. Alternatively, the solution can be graphically determined by the intersection of $a_n = T - d_n$ and $a_{n+1} = f(d_n)$, as shown in Fig. 2(A). If a small perturbation, δd_n or δa_n, is given to the steady state at the nth beat, then from Eq. (18), one obtains the APD change for the $(n+1)$th beat as

$$\delta a_{n+1} = \frac{df}{dd_n}\delta d_n = -\frac{df}{dd_n}\delta a_n. \tag{19}$$

The steady state becomes unstable when the slope of APD restitution curve at the steady state is greater than 1 (or less than −1), i.e.,

$$|f'| = \left|\frac{df}{dd_n}\right| > 1, \tag{20}$$

since the perturbation grows instead of shrinks. For $f' > 1$, a period doubling bifurcation leads to APD alternans, as indicated by the perturbation in Eq. (19) growing in an alternating (positive-negative) pattern until a stationary alternans is established due to nonlinearity of the APD restitution curve. For $f' < -1$, a saddle-node bifurcation occurs: the perturbation grows steadily until the system reaches a new steady state.

For the steeper monotonic APD restitution curve in Fig. 2(A), $f' = 1$ occurs at $d = 90$ ms [Fig. 2(B)] at which $a = 185$ ms. APD alternans occurs at $T = 90$ ms + 185 ms = 275 ms [Fig. 2(C)]. As T decreases, 2:1 block occur at $T = 226$ ms, followed by a more complex response, such as chaos. The bifurcation sequence shows: $1:1 \rightarrow 2:2 \rightarrow 2:1 \rightarrow 4:2 \rightarrow \text{ID} \rightarrow 4:1 \rightarrow 8:2 \rightarrow \text{ID}$. This bifurcation sequence is very similar to the one observed in an experiment by Chialvo *et al.* [26], in which a bifurcation sequence, $1:1 \rightarrow 2:2 \rightarrow 2:1 \rightarrow 4:2 \rightarrow 3:1 \rightarrow 6:2 \rightarrow 4:1 \rightarrow 8:2 \rightarrow \text{ID}$, was observed. For the shallower APD restitution curve shown in Fig. 2(A), as T decreases, neither alternans nor other complex dynamics occur, except for 2:1 and 3:1 block [Fig. 2(D)], etc. In this case, 2:1 block occurs at $T = 110$ ms, which is much shorter than in the steep APD restitution case. The occurrence of chaos for monotonic APD restitution curves is a consequence of both steep APD restitution and stimulation failure, producing a classical shift map mechanism of chaos as indicated by the return map shown in Fig. 2(E).

For nonmonotonic APD restitution curves [Fig. 3(A)], both $f' > 1$ and $f' < -1$ can occur [Fig. 3(B)], leading to multiple steady state solutions [inset in Fig. 3(A)] as T deceases. In Fig. 3(C), a bistable solution (dashed box) occurs at around $T = 250$ ms, followed by a period doubling route to chaos [Fig. 3(C)]. Unlike the case of monotonic APD restitution curve, chaos can precede 2:1 block. Before 2:1 block, this mechanism for chaos is the same as for the unimodal map [Fig. 3(E)], but after 2:1 block, both shift map and unimodal map mechanisms may be responsible, as shown by the return maps in Fig. 3(D).

IV. DYNAMICAL INSTABILITIES DUE TO INTRACELLULAR CALCIUM CYCLING

In this section, we investigate the nonlinear dynamics of Ca cycling under two conditions: (1) Total Ca inside the cell is set to a constant, i.e., Ca influx exactly matches the Ca efflux at any time and condition. (2) Total Ca in the cell can vary on a beat-to-beat basis, as occurs physiologically under voltage or action potential clamp conditions. Although the first case is not physiologically realistic with current technology, it is important for understanding the dynamical effects due to intracellular Ca cycling alone.

A. Ca cycling dynamics when total Ca is constant

Ca cycling dynamics for constant total Ca has been analyzed by Shiferaw *et al.* [14] in general and in a linear map

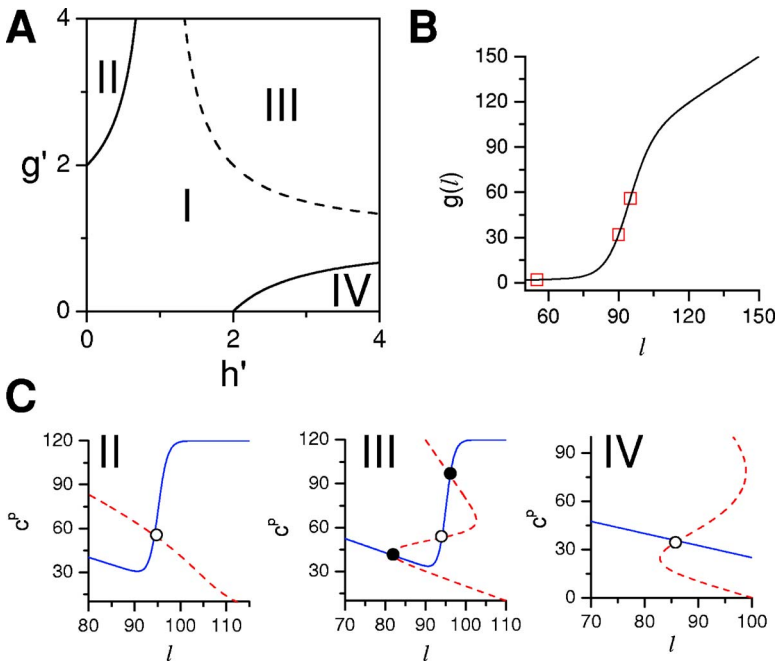

FIG. 4. (Color online) (A) Phase diagram in the parameter space of steepness of SR Ca release and uptake curves. Solid line is $(1-h')(1-g') = -1$ and dashed line is $(1-h')(1-g') = 1$. Based on available experimental information, only the positive slopes (shaded area) are realistic parameters. Region I is a region with one stable steady state solution. Regions II and IV exhibit alternans and other complex dynamics. Region III is bistable. (B) Symbols are data from experiments of Basani *et al.* [43] and the line shows the plot of $g(l_n) = l_n[1-(1-0.036)/(1+e^{(l_n-93.5)/5})]$. (C) Examples of nullclines when parameters are set in regions II, III, and IV. Solid line is a plot of Eq. (22) and the dashed line is a plot of Eq. (25).

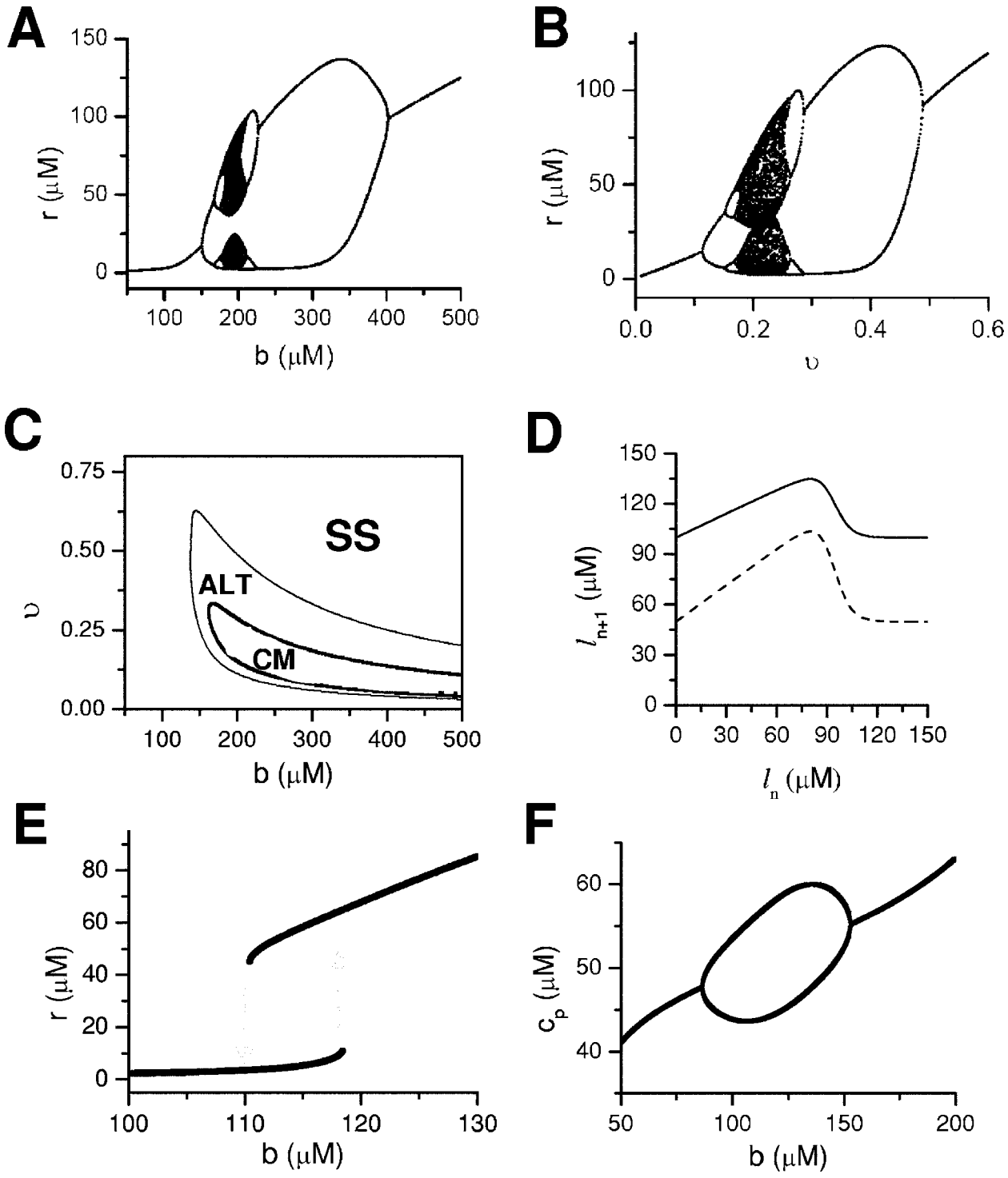

FIG. 5. Dynamics due to nonlinear SR Ca release and uptake when total cell Ca is constant. (A) Ca release (r) versus total Ca (b) for $\upsilon=0.25$. (B) SR Ca release (r) versus the rate of SR Ca uptake (υ) for $b=200$. (C) Phase diagram in the υ-b parameter space. "SS" is the stable steady state region, "ALT" is the alternans region, and "CM" is the complex dynamics region, including higher periodic and chaotic solutions. (D) Return maps (l_{n+1} vs l_n) for $\upsilon=0.25$ (dashed) and $\upsilon=0.5$ (solid), showing unimodal maps and chaos occurring when the slopes are steep (dashed). $g(l_n)=l_n[1-(1-0.036)/(1+e^{(l_n-93.5)/5})]$ and $h(c^p_{n+1})=\upsilon c^p_{n+1}[1-1/(1+e^{(c^p_{n+1}-50)/20})]$ were used for (A)–(D), representing transitions from region I to region II of Fig. 4(A). (E) A bistable solution when the parameters are set to undergo a transition from region I to region III in Fig. 4(A). $g(l_n)=l_n[1-(1-0.036)/(1+e^{(l_n-93.5)/5})]$ and $h(c^p_{n+1})=\upsilon c^p_{n+1}[1-1/(1+e^{(c^p_{n+1}-50)/4})]$ were used with $\upsilon=0.75$. Dashed arrows indicate that for continuously increasing or decreasing b, the system jumps from one steady state to the other at different thresholds. (F) SR Ca release (r) versus total Ca (b) when the parameters are set to undergo transition from region I to region IV in Fig. 4(A). $g(l_n)=0.25l_n$ and $h(c^p_{n+1})=\upsilon c^p_{n+1}[1-1/(1+e^{(c^p_{n+1}-50)/4})]$ were used with $\upsilon=0.75$.

by Weiss *et al.* [15]. Here we extend their analysis to include both SR Ca release and SR Ca uptake using more realistic nonlinear functions. When the total Ca inside the cell is constant, i.e., $b_n=b$, only one iterated map [Eq. (8)] is needed to describe the dynamics, which is

$$l_{n+1} = l_n - g(l_n) + h(c^p_{n+1}), \tag{21}$$

where c^p_{n+1} can be obtained from Eqs. (5) and (6) as

$$c^p_{n+1} = b - l_n + g(l_n). \tag{22}$$

A small perturbation from the steady state satisfies the following equation:

$$\delta l_{n+1} = \delta l_n - g'\,\delta l_n + h'\frac{dc^p_{n+1}}{dl_n}\delta l_n = (1-h')(1-g')\,\delta l_n \tag{23}$$

in which $h' = \frac{dh(c^p_{n+1})}{dc^p_{n+1}}$ and $g' = \frac{dg(l_n)}{dl_n}$ are the slopes of the SR Ca release function and SR Ca uptake function at steady state. Therefore the steady state is stable when

$$|(1-h')(1-g')| > 1. \tag{24}$$

Otherwise, the steady state is unstable. In the parameter space of the two slopes (g' and h'), the stable and unstable regions are separated by hyperbolic lines of $(1-h')(1-g')=-1$ and $(1-h')(1-g')=1$. Available experimental data indicates that under physiological conditions, $g'>0$ and $h'>0$, so that we only show positive parameter ranges in Fig. 4(A). The experimental data obtained by Bassani *et al.* [43] for SR Ca release can be fit by $g(l_n)=l_n[1-(1-0.036)/(1+e^{(l_n-93.5)/5})]$ [Fig. 4(B), after Shannon *et al.* [44]], and is used in the simulations in this paper unless otherwise indicated. For the SR Ca uptake function $h(c^p_{n+1})$, experimental data [49,50] suggests a sigmoidal function of Ca, although no direct data is available. As an approximation, we use $h(c^p_{n+1})=\upsilon c^p_{n+1}[1-1/(1+e^{(c^p_{n+1}-50)/20})]$ in the simulations, unless otherwise indicated.

Combining Eq. (21) with Eq. (22), we obtain an equation for l_{n+1} as a function of c^p_{n+1}, i.e.,

$$l_{n+1} = b + h(c^p_{n+1}) - c^p_{n+1}. \tag{25}$$

Equation (22) and Eq. (25) are two nullclines in the space of SR Ca load (l) and peak cytoplasmic Ca (c^p), and their intersections are the steady state solutions. Figure 4(C) shows three examples in which the parameters were set in regions II, III or IV of Fig. 4(A), respectively. In region I of Fig. 4(A), the steady state is stable. When the parameters change from region I to region II, a period-doubling bifurcation leading to alternans and chaos is observed [Figs. 5(A)–5(C)]. Figure 5(A) illustrates the period-doubling bifurcation for increasing total Ca b with the SR Ca uptake rate υ fixed. Figure 5(B) shows the bifurcation generated by changing SR Ca uptake rate υ while keeping total Ca b fixed. Figure 5(C) shows the phase diagram for alternans and complex dynamics in the parameter space of SR Ca uptake rate υ versus total Ca b. The mechanism for chaos is the same as in the logistic map, i.e., a unimodal map with steep slopes [Fig. 5(D)]. When the parameters change from region I to region III of Fig. 4(A), a saddle-node bifurcation causes the system to bifurcate from one stable steady state to three steady state solutions [Fig. 4(A)], two of which are stable and one unstable, leading to bistability as h' and g' increase or total Ca increases [Fig. 5(E)]. When the parameters change from region I to region IV of Fig. 4(A), a bifurcation to Ca alternans was observed [Fig. 5(F)]. In this case, alternans can be caused by steep SR Ca uptake without the need for steep SR Ca release.

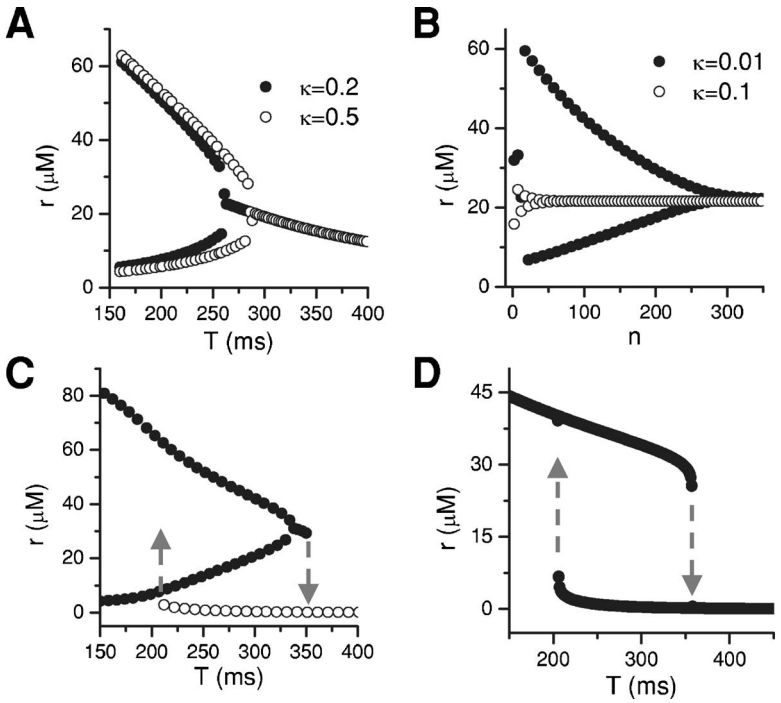

FIG. 6. Ca dynamics during simulated action potential voltage clamp conditions, from Eq. (26). (A) SR Ca release r versus pacing cycle length T for two different values of κ. The same $g(l_n)$ and $h(c^p_{n+1})$ as in Fig. 5(A) were used with $\upsilon=0.4$ and $c(T)=28(1+2e^{-T/300})$. (B) SR Ca release r versus beat number for $T=275$ ms for two different small values of κ. (C) SR Ca release r versus pacing cycle length T. The same $g(l_n)$ and $h(c^p_{n+1})$ as in Fig. 5(B) were used with $\upsilon=0.4$. $\kappa=0.2$, and $c(T)=20(1+2e^{-T/300})$. (D) SR Ca release r versus pacing cycle length T. The same $g(l_n)$ and $h(c^p_{n+1})$ as in Fig. 5(F) were used with $\upsilon=0.4$. $\kappa=0.2$, and $c(T)=20(1+2e^{-T/300})$. Dashed arrows in (C) and (D) indicate discontinuous transitions with continuously increasing or decreasing T.

Physiologically, the transition from a stable steady state to alternans due to parameter changes from region I to region II may correspond to two conditions. The first is the alternans observed in normal cardiac myocytes or tissue at rapid heart rates [54]. In this case, as cycle length T deceases, Ca accumulates in the cell and thus the total Ca increases, engaging the steeply sloped region of SR Ca release versus SR Ca load relationship. The second is the alternans due to depressed SERCA pump in acute myocardial ischemia or heart failure [55,56]. In this case, SR Ca uptake is reduced due to depressed SERCA pump function [57], while steep SR Ca release may still be preserved at smaller SR Ca loads [58]. Alternans is also promoted by drugs that reduce the SR Ca pump [59]. The transition to alternans due to parameter changes from region I to region IV may correspond to the case in which SR Ca release is depressed pharmacologically by the drug tetracaine [34]. Further modeling and experimental studies are needed to validate the conclusions of this iterated map analysis.

B. Ca cycling dynamics under action potential voltage clamp

In real cells, Ca enters and exits the cell during each action potential through L-type Ca channels, Na-Ca exchange and other processes, so that total Ca is not necessarily constant. Here we investigate the case in which total cell Ca is allowed to vary on a beat-to-beat basis, corresponding, for example, to pacing with an action potential voltage clamp. In this setting, the membrane potential of the cell is externally clamped with the waveform of a normal action potential applied periodically with period T.

In the first case, we assume SR Ca release and uptake are independent of activation rate, so that the mapping equations are [from Eqs. (8) and (16)],

$$l_{n+1} = l_n - g(l_n) + h(c^p_{n+1}),$$

$$b_{n+1} = b_n - \kappa[c_n - c(T)]. \tag{26}$$

We first carry out a linear stability analysis of the steady state for Eq. (26). The linearized equations become

$$\begin{pmatrix} \delta l_{n+1} \\ \delta b_{n+1} \end{pmatrix} = \begin{pmatrix} (1-h')(1-g') & h' \\ \kappa & 1-\kappa \end{pmatrix} \begin{pmatrix} \delta l_n \\ \delta b_n \end{pmatrix}. \tag{27}$$

The stability of the state is determined by the eigenvalues of the Jacobian in Eq. (27), which are

$$\lambda_{1,2} = \frac{(1-h')(1-g') + 1 - \kappa \pm \sqrt{[(1-h')(1-g') - (1-\kappa)]^2 + 4\kappa h'}}{2} = \frac{\lambda_0 + 1 - \kappa \pm \sqrt{(\lambda_0 - 1 + \kappa)^2 + 4\kappa h'}}{2} \tag{28}$$

in which $\lambda_0 = (1-h')(1-g')$ is the eigenvalue when total cell Ca is constant. For $\lambda_0 \ll 1$, and $\kappa \ll 1$, Eq. (28) can be approximated by

$$\lambda_1 = \lambda_0 - \kappa h', \quad \lambda_2 = 1 - \kappa + \kappa h'. \tag{29}$$

Therefore, for small κ, λ_1 in Eq. (29) is mainly determined by SR Ca cycling dynamics, whereas λ_2 is mainly determined by the membrane Ca flux. When $h' < 1$, $\lambda_2 < 1$ always holds, whereas λ_1 may become smaller than -1 if λ_0 is close to -1. In other words, Ca flux through the membrane can promote Ca alternans. When $h' > 1$, λ_2 becomes greater than one, leading to new instabilities. It should be noted that when κ is small, λ_2 is close to one, which indicates that following a perturbation, a long time is required for the system to return to its stationary state. In other words, κ is the parameter determining the memory for Ca dynamics. Short-term memory has shown to be an important feature in cardiac systems [60–62]: the small beat-to-beat Ca extrusion or accumulation may contribute importantly for cardiac memory [41].

We numerically simulated Eq. (26) to verify the theoretical analysis. Figure 6(A) shows bifurcation diagrams for $\kappa = 0.2$ and $\kappa = 0.5$ with the parameters chosen for the transition from region I to region II of Fig. 4(A), at which $h' < 1$. Ca alternans occurs at a longer cycle length T as κ becomes larger. Figure 6(B) compares the times for the system to evolve to a steady state from initial conditions far away from the steady state, for two different κ. It takes more time for the system to evolve to its steady state for smaller κ, illustrating how κ regulates the time constant of memory of the system. If we set the parameters for Ca cycling undergoing a transition from region I to region III of Fig. 4(A) at which $h' > 1$ and g' is also large, the bifurcation pattern is very different from when the total cell Ca is constant [Fig. 6(C)]. In this case, at long T, a single stable steady state with very small SR Ca release exists, whereas at short T, alternans occurs. In the intermediate T range, alternans and the low SR Ca release steady state coexist, creating a form of bistability. When we set the parameters for Ca cycling undergoing a transition from region I to region IV of Fig. 4(A), at which $h' > 1$, the bifurcation to alternans in the constant total Ca case is converted into a saddle-node bifurcation leading to bistability [Fig. 6(D)]. Thus, the numerical results in Fig. 6 agree with the eigenvalue analysis above.

In the second case, we allow SR Ca release and uptake to be rate dependent. The map equations then become

$$l_{n+1} = l_n - q(d_n)g(l_n) + u(T)h(c^p_{n+1}),$$

$$b_{n+1} = b_n - \kappa[c_n - c(T)]. \tag{30}$$

We first study how restitution properties of SR Ca release affect the dynamics. Figure 7(A) shows bifurcation diagrams

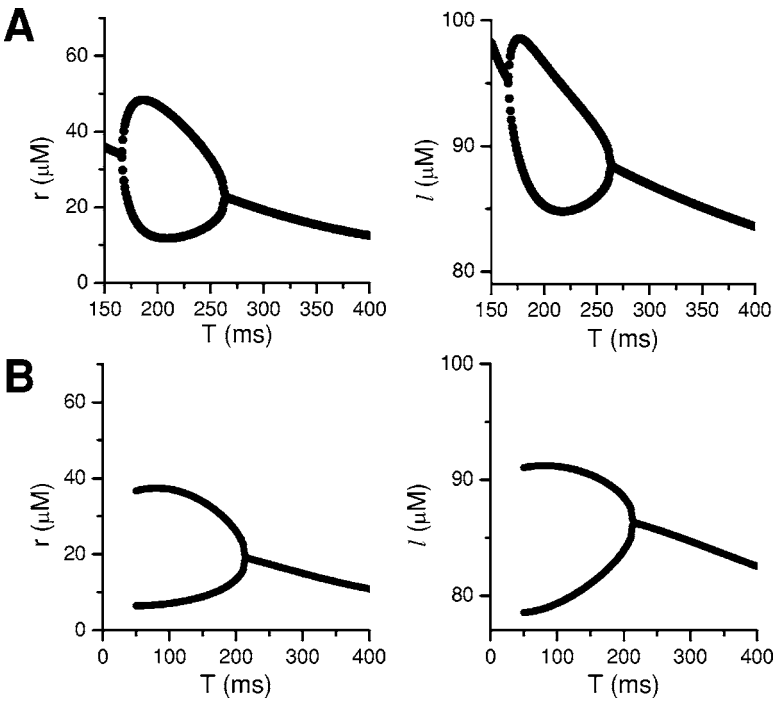

FIG. 7. Effects of rate-dependent SR Ca release and uptake on Ca dynamics during simulated action potential voltage clamp conditions, from Eq. (30). $c(T)=28(1+2e^{-T/300})$, and $g(l_n)$ and $h(c^p_{n+1})$ are the same as in Fig. 5(A). Left-hand panels: SR Ca release versus pacing cycle length T. Right-hand panels: SR Ca load versus pacing cycle length T. $\upsilon=0.4$, $\kappa=0.2$. (A) For $q(d_n)=(1-0.5e^{-d_n/80})$, $u(T)=1$ and $d_n=T-150$. (B) For $u(T)=(1-0.5e^{-T/200})$ and $q(d_n)=1$.

of SR Ca release and SR Ca load by simulating Eq. (30) with $u(T)=1$ and the parameters were set so that a transition occurs from region I to region II of Fig. 4(A). As T decreases, Ca alternans occurs and then disappears. Although the SR Ca release function is attenuated as T decreases, the actual SR Ca release in the model does not decrease due to the increased SR Ca load. We also simulated Eq. (30) with $q(d_n)=1$ to study how rate-dependent SR Ca uptake will affect the dynamics. Figure 7(B) shows that for this case, Ca alternans with an attenuated amplitude occurs at shorter T [compare to Fig. 6(A)], indicating that rate-dependent SR Ca uptake tends to stabilize the system. This seems to be opposite to the phase diagram of Fig. 4(A), in which once the parameters are set to region I with steep SR Ca release, decreasing SR Ca uptake rate promotes alternans. This is because as T decreases, $u(T)$ decreases, but so does the SR Ca load, pushing the system into the region with less steep SR Ca release (smaller g'). This latter effect suppresses alternans.

V. DYNAMICS OF EC COUPLING

After analyzing the APD and Ca cycling dynamics separately above, here we couple the APD map with the Ca cycling maps to study the combined dynamics of EC coupling. The main iterated map equations are

$$a_{n+1}=f(d_n)+p(c^p_{n+1})a_{n+1},$$

$$l_{n+1}=l_n-q(d_n)g(l_n)+u(T)h(c^p_{n+1}),$$

$$b_{n+1}=b_n+\eta(a_{n+1}-a_n)-\kappa[c_n-c(T)], \tag{31}$$

as defined in Eqs. (1)–(17) in the model development section. For the convenience of analytical treatment of stability, we first assume that the total Ca in the cell is constant for each beat, so that we can reduce Eq. (31) into two equations, i.e.,

$$a_{n+1}=f(d_n)+p(c^p_{n+1}),$$

$$a_{n+1}=\frac{1}{1-p(c^p_{n+1})}f(d_n),$$

$$l_{n+1}=l_n-q(d_n)g(l_n)+u(T)h(c^p_{n+1}). \tag{32}$$

Linearizing Eq. (32) at its steady state, we have

$$\delta a_{n+1}=\frac{-(1-\gamma c_{pn+1})f'\,\delta a_n+\gamma(-1+qg')f\delta l_n}{(1-\gamma c^p_{n+1})^2}=m_{11}\delta a_n+m_{12}\delta l_n,$$

$$\delta l_{n+1}=gq'\,\delta a_n+(1-qg')[1-u(T)h']\delta l_n=m_{21}\delta a_n+m_{22}\delta l_n \tag{33}$$

in which $q'=\frac{dq(d_n)}{dd_n}$ is the slope of the SR Ca release restitution. All variables, functions, and derivatives in Eq. (33) are their values at the steady state. The two eigenvalues of Eq. (33) are

$$\lambda_{1,2}=\frac{(m_{11}+m_{22})\pm\sqrt{(m_{11}-m_{22})^2+4m_{12}m_{21}}}{2}, \tag{34}$$

$m_{11}=-\frac{f'}{1-\gamma c^p_{n+1}}$ is the contribution from the APD restitution, and $m_{22}=(1-qg')[1-u(T)h']$ is the contribution from the Ca cycling. m_{12} and m_{21} are the contributions from the couplings of APD and Ca.

As shown by Shiferaw *et al.* [16], depending on coupling relation γ between APD and Ca in Eq. (4), different dynamics occurs. Ca can influence APD positively when $\gamma>0$ (i.e., a larger Ca transient causes APD to shorten, termed *positive*

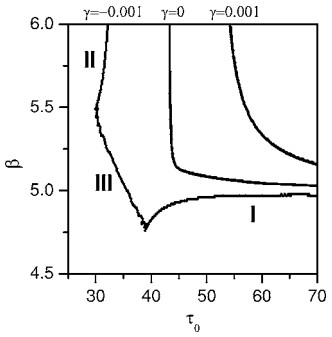

FIG. 8. Stability boundaries for positive Ca-to-APD coupling ($\gamma=0.001$), uncoupled ($\gamma=0$), negative Ca-to-APD coupling ($\gamma=-0.001$). $T=250$ ms. The parameters for APD restitution are the same as in Fig. 2(B), and the parameters for Ca cycling are the same as in Fig. 5(A) except β and τ_0. $c(T)=28(1+2e^{-T/300})$, $q(d_n)=(1-0.5e^{-d_n/80})$, and $u(T)=(1-0.15e^{-T/200})$ were used.

Ca-to-APD coupling), in which case the coupling promotes instability. Alternatively, Ca can influence APD negatively when $\gamma<0$ (i.e., a larger Ca transient causes APD to shorten, termed *negative* Ca-to-APD coupling), in which case the coupling suppresses instability. However, new dynamics also can occur in the negative Ca-to-APD coupling case, including electromechanically concordant alternans (long APD accompanying a large Ca transient and vice versa), electromechanically discordant alternans (long APD accompanying a small Ca transient and vice versa), or electromechanically quasiperiodic oscillations. Based on Eq. (34), the occurrence of quasiperiodicity requires $m_{12}m_{21}=\gamma q' g(qg'-1)f<0$, which can occur only in the negative Ca-to-APD coupling case in which $\gamma<0$.

Numerical simulation of Eq. (31) verifies the Ca-to-APD coupling effects shown by the eigenvalue analysis. Figure 8 shows the instability boundaries for different Ca-to-APD coupling ($\gamma=-0.001$, 0, and 0.001, respectively), which is the same as shown previously by Shiferaw *et al.* [16]. Positive Ca-to-APD coupling destabilizes the system (pushing the border upwards to the right) while negative Ca-to-APD coupling stabilizes the system (pushing the border down to the left). For negative Ca-to-APD coupling, there are three instability boundaries. At boundary I, the instability is mainly due to the steepness of the SR Ca release function g', and leads to electromechanically discordant alternans [Fig. 9(A)]. At boundary II, the instability is mainly due to the steepness of the APD restitution curve, and it first leads to electromechanically concordant alternans, followed by electromechanically discordant alternans after stimulation failure, and finally to chaos [Fig. 9(B)]. At boundary III, both

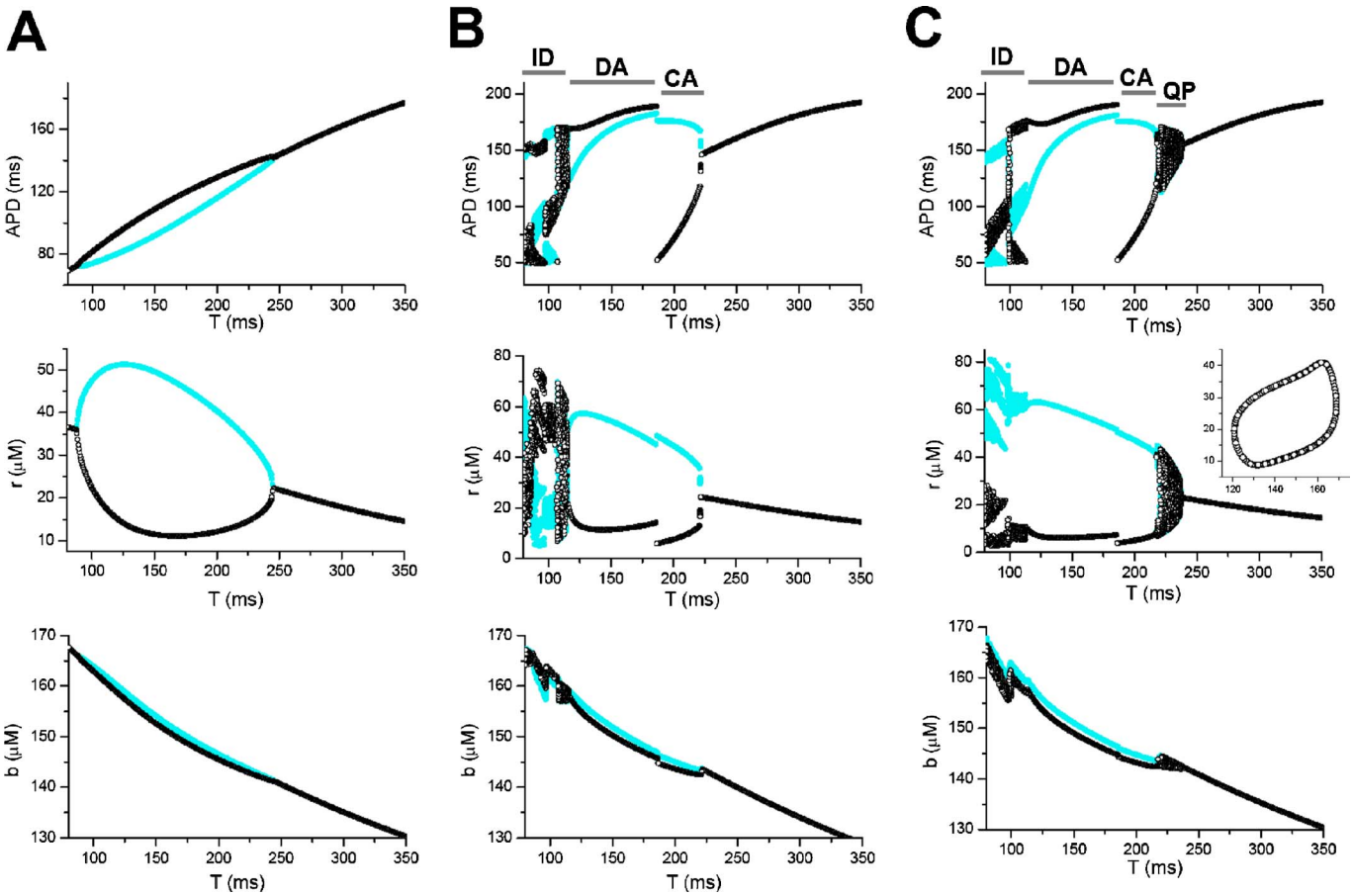

FIG. 9. (Color online) Bifurcations for negative Ca-to-APD coupling ($\gamma=-0.002$) through the three stability boundaries shown in Fig. 8. Black represents odd beats and cyan, even beats. (A) $\tau_0=60$, $\beta=5$ (boundary I). (B) $\tau_0=30$, $\beta=6$ (boundary II). (C) $\tau_0=30$, $\beta=5$ (boundary III). ID represents irregular dynamics; CA represents concordant alternans; DA represents discordant alternans; QP represents quasiperiodicity. In the inset of the second panel in (C), a quasiperiodic relation between SR Ca release r (y axis) and APD (x axis) is shown.

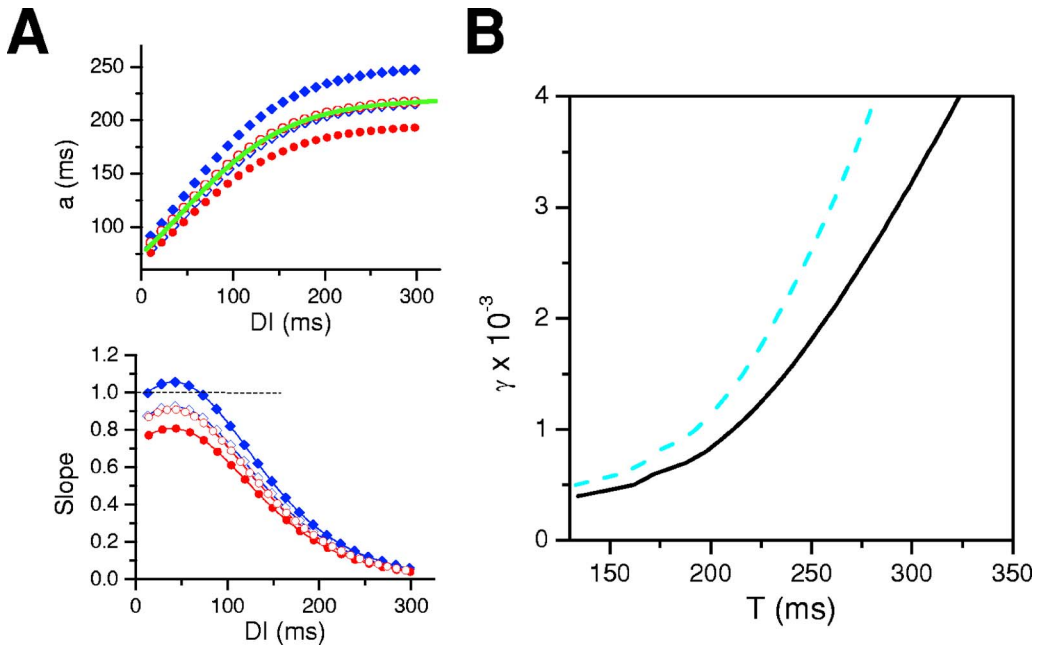

FIG. 10. (Color online) (A) APD versus DI for positive Ca-to-APD coupling (γ=0.001) with (open diamonds) and without (solid diamonds) APD normalized to 220 ms; for negative Ca-to-APD coupling (γ=−0.001) with (open circles) and without (solid circles) APD normalized; and for uncoupled system (line). τ_0=60 and β=8. (B) Stability boundaries before (solid line) and after (dashed line) APD normalization. Other parameters are the same as in Fig. 8.

voltage and Ca cycling dynamics are unstable. In this case, quasiperiodic dynamics occurs close to the bifurcation, followed by electromechanically concordant alternans, electromechanically discordant alternans, and finally chaos [Fig. 9(C)].

In this model, negative Ca-to-APD coupling shortens APD and positive Ca-to-APD coupling prolongs APD, which in turn affects APD restitution slope [Fig. 10(A)] and thus the onset of the instability. To exclude the possibility that these effects on APD restitution slope caused the shift in instability boundaries, Fig. 10(B) shows the instability boundaries for the positive Ca-to-APD coupling case before and after the baseline APD was rescaled. Prolongation of APD by positive coupling promotes instability, but the coupling itself has a large effect on stability.

We also set the parameters for Ca cycling so as to undergo transitions from regions I to regions III and IV of Fig. 4(A). We were not able to identify dynamics due to the coupling, although the dynamics is very complex when both subsystems are unstable. However, we believe other dynamics may emerge due to the high-dimensional parameters and nonlinearity.

Finally we studied the effects of APD on Ca flux into the cell, i.e., the effects of the term $\eta(a_{n+1}-a_n)$ in Eq. (31). When $\eta>0$, this term indicates that a longer APD causes net Ca influx, which we call *positive* APD-to-Ca coupling. When $\eta<0$, this term indicates that a longer APD causes net Ca efflux, which we call *negative* APD-to-Ca coupling. Figure 11(A) shows the instability boundaries when these two cases of APD-to-Ca coupling are matched with either positive (solid line) or negative (dashed line) Ca-to-APD coupling. Figure 11(B) shows SR Ca release versus APD for the four different regions marked in Fig. 11(A). Quasiperiodic dynamics occurs both with the combination of negative APD-to-Ca coupling with positive Ca-to-APD coupling, as well as positive APD-to-Ca coupling with negative Ca-to-APD coupling.

VI. DISCUSSION

In this study, we developed a set of nonlinear iterated map equations, based on data obtained from experimental studies, to describe the nonlinear dynamics of EC coupling. Saddle-node bifurcations leading to bistability, period-doubling bifurcations leading to alternans, and period-doubling routes to chaos can independently occur in both APD or Ca cycling subsystems. The mechanisms of the dynamics due to APD restitution are well understood from previous studies [3,42,51,53,63]. Whereas some of the mechanisms for dynamics of Ca cycling and its coupling to APD have been analyzed previously [13–16], the saddle-node bifurcations leading to bistability and period-doubling routes to chaos have not been previously described for either Ca cycling alone, or for the coupled dynamics of APD and Ca cycling, and represent findings of the present study. Most significantly, our study extends the analysis of EC coupling nonlinear dynamics to the case in which total cell Ca varies from beat-to-beat. This takes an important step in linking the coupled maps analysis to physiologically realistic conditions, since in experimental studies, total cell Ca always changes on a beat-to-beat basis, except for the trivial case of period-1. Under these conditions, we show that the coupling between APD and Ca can lead to electromechanically discordant APD-Ca alternans or quasiperiodicity, depending on whether the Ca-to-APD or APD-to-Ca couplings are both negative, both positive or opposite in sign.

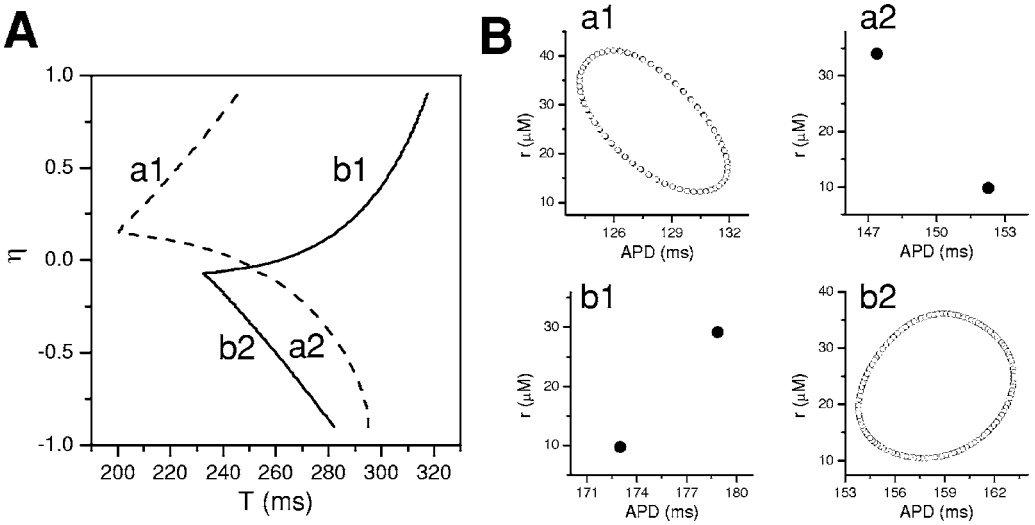

FIG. 11. (A) The stability boundaries in η-T parameter space for γ=0.001 (solid line) and γ=−0.001 (dashed line). (B) r versus APD at the four boundary locations marked "$a1$," "$a2$," "$b1$," and "$b2$." τ_0=60, β=5, and other parameters are the same as in Fig. 8.

However, although the iterated map approach has the advantage of being easy for analytical and numerical treatment and for obtaining mechanistic insights into dynamics, it has limitations. It still remains a low-dimensional representation of a high-dimensional system, which may not accurately represent the dynamics of the real system or may miss important dynamics. For these reasons, it will be critical to validate the dynamics using detailed physiological action potential models, to both define the dynamics that are relevant physiologically, and to assess how additional factors in detailed models may alter dynamics predicted by the iterated map. For instance, short-term memory due to ion channel recovery and ion accumulation may have large effects on dynamics [60,61,64–66]. In addition, as shown by Jordan and Christini [67], action potential morphology may modulate the onset of Ca alternans, which we cannot assess in the iterated map study. Nevertheless, the iterated map study provides potentially useful mechanistic insights to EC coupling dynamics, as exemplified originally by Nolasco and Dahlen [3] in their classic study of APD restitution. The approach here provides valuable information which can be used as a basis to explore dynamical features of more detailed models, to illuminate experimental findings and to design experimentally testable predictions for new biological experiments. For example, whereas early interpretations of experimental Ca transient alternans focused on the sensitivity of SR Ca release (our g' factor) as driving alternans [13,68], the iterated map studies also demonstrate a key role of SR Ca uptake (our h' factor). This is likely to be the more important factor in causing alternans during ischemia and heart failure [15], in which the major pathophysiological change is depression of SERCA function, more so than altered gain of SR Ca release [equivalent to the transition from region I to region II in Fig. 4(A)]. Our study also shows that depression of SR Ca release can promote alternans when SR Ca uptake is normal [transition from region I to region IV in Fig. 4(A)], which may provide an explanation for why tetracaine, which inhibits RyR opening, promotes Ca alternans [34].

ACKNOWLEDGMENTS

Supported by NIH/NHLBI P01 HL078931, and the Laubisch and Kawata endowments.

[1] J. N. Weiss, Z. Qu, P. S. Chen *et al.*, Circulation **112**, 1232 (2005).
[2] Z. Qu and J. N. Weiss, J. Cardiovasc. Electrophysiol. **17**, 1042 (2006).
[3] J. B. Nolasco and R. W. Dahlen, J. Appl. Physiol. **25**, 191 (1968).
[4] A. Karma, Chaos **4**, 461 (1994).
[5] M. Courtemanche, Chaos **6**, 579 (1996).
[6] Z. Qu, J. N. Weiss, and A. Garfinkel, Am. J. Physiol. **276**, H269 (1999).
[7] M. L. Riccio, M. L. Koller, and R. F. Gilmour, Jr., Circ. Res. **84**, 955 (1999).
[8] A. Garfinkel, Y. H. Kim, O. Voroshilovsky *et al.*, Proc. Natl. Acad. Sci. U.S.A. **97**, 6061 (2000).
[9] Z. Qu, F. Xie, A. Garfinkel *et al.*, Ann. Biomed. Eng. **28**, 755 (2000).
[10] M. H. Lee, S. F. Lin, T. Ohara *et al.*, Am. J. Physiol. Heart Circ. Physiol. **280**, H2689 (2001).
[11] I. Banville and R. A. Gray, J. Cardiovasc. Electrophysiol. **13**, 1141 (2002).
[12] T. J. Wu, S. F. Lin, A. Baher *et al.*, Circulation **110**, 2110 (2004).
[13] D. A. Eisner, H. S. Choi, M. E. Diaz *et al.*, Circ. Res. **87**, 1087 (2000).
[14] Y. Shiferaw, M. A. Watanabe, A. Garfinkel *et al.*, Biophys. J. **85**, 3666 (2003).

[15] J. N. Weiss, A. Karma, Y. Shiferaw *et al.*, Circ. Res. **98**, 1244 (2006).
[16] Y. Shiferaw, D. Sato, and A. Karma, Phys. Rev. E **71**, 021903 (2005).
[17] D. Sato, Y. Shiferaw, A. Garfinkel *et al.*, Circ. Res. **99**, 520 (2006).
[18] J. M. Cao, Z. Qu, Y. H. Kim *et al.*, Circ. Res. **84**, 1318 (1999).
[19] Z. Qu, A. Garfinkel, P. S. Chen *et al.*, Circulation **102**, 1664 (2000).
[20] M. A. Watanabe, F. H. Fenton, S. J. Evans *et al.*, J. Cardiovasc. Electrophysiol. **12**, 196 (2001).
[21] D. M. Bers, *Excitation-Contraction Coupling and Cardiac Contractile Force* (Kluwer Academic, Dordrecht, 2001).
[22] D. M. Bers, Nature (London) **415**, 198 (2002).
[23] M. R. Guevara, L. Glass, and A. Shrier, Science **214**, 1350 (1981).
[24] D. R. Chialvo and J. Jalife, Nature (London) **330**, 749 (1987).
[25] L. H. Frame and M. B. Simson, Circulation **78**, 1277 (1988).
[26] D. R. Chialvo, R. F. Gilmour, and J. Jalife, Nature (London) **343**, 653 (1990).
[27] J. M. Davidenko, A. M. Pertsov, R. Salomonsz *et al.*, Nature (London) **355**, 349 (1992).
[28] P. Lipp and E. Niggli, Biophys. J. **65**, 2272 (1993).
[29] A. Garfinkel, P. S. Chen, D. O. Walter *et al.*, J. Clin. Invest. **99**, 305 (1997).
[30] R. A. Gray, A. M. Pertsov, and J. Jalife, Nature (London) **392**, 75 (1998).
[31] J. M. Pastore, S. D. Girouard, K. R. Laurita *et al.*, Circulation **99**, 1385 (1999).
[32] J. Huser, Y. G. Wang, K. A. Sheehan *et al.*, J. Physiol. (London) **524**, 795 (2000).
[33] Y. W. Qian, W. T. Clusin, S. F. Lin *et al.*, Circulation **104**, 2082 (2001).
[34] M. E. Diaz, D. A. Eisner, and S. C. O'Neill, Circ. Res. **91**, 585 (2002).
[35] J. Kockskamper and L. A. Blatter, J. Physiol. (London) **545**, 65 (2002).
[36] S.-M. Hwang, T. Y. Kim, and K. J. Lee, Proc. Natl. Acad. Sci. U.S.A. **102**, 10363 (2005).
[37] M. Courtemanche, L. Glass, and J. P. Keener, Phys. Rev. Lett. **70**, 2182 (1993).
[38] V. Elharrar and B. Surawicz, Am. J. Physiol. **244**, H782 (1983).
[39] M. R. Franz, J. Schaefer, M. Schottler *et al.*, Circ. Res. **53**, 815 (1983).
[40] M. L. Koller, M. L. Riccio, and R. F. Gilmour, Jr., Am. J. Physiol. **275**, H1635 (1998).
[41] J. I. Goldhaber, L. H. Xie, T. Duong *et al.*, Circ. Res. **96**, 459 (2005).
[42] M. Watanabe, N. F. Otani, and R. F. Gilmour, Circ. Res. **76**, 915 (1995).
[43] J. W. Bassani, W. Yuan, and D. M. Bers, Am. J. Physiol. **268**, C1313 (1995).
[44] T. R. Shannon, K. S. Ginsburg, and D. M. Bers, Biophys. J. **78**, 334 (2000).
[45] H. Cheng, M. R. Lederer, W. J. Lederer *et al.*, Am. J. Physiol. **270**, C148 (1996).
[46] E. A. Sobie, L. S. Song, and W. J. Lederer, J. Cardiovasc. Electrophysiol. **17**, S64 (2006).
[47] T. R. Shannon, K. S. Ginsburg, and D. M. Bers, Circ. Res. **91**, 594 (2002).
[48] W. G. Wier and D. T. Yue, J. Physiol. (London) **376**, 507 (1986).
[49] J. W. Bassani, R. A. Bassani, and D. M. Bers, J. Physiol. (London) **476**, 279 (1994).
[50] L. Hove-Madsen and D. M. Bers, Circ. Res. **73**, 820 (1993).
[51] M. Delmar, D. C. Michaels, and J. Jalife, Circ. Res. **65**, 761 (1989).
[52] A. Vinet, D. R. Chialvo, D. C. Michaels *et al.*, Circ. Res. **67**, 1510 (1990).
[53] T. J. Lewis and M. R. Guevara, J. Theor. Biol. **146**, 407 (1990).
[54] E. Chudin, J. Goldhaber, A. Garfinkel *et al.*, Biophys. J. **77**, 2930 (1999).
[55] H. C. Lee, R. Mohabir, N. Smith *et al.*, Circulation **78**, 1047 (1988).
[56] P. S. Petkova-Kirova, E. Gursoy, H. Mehdi *et al.*, Am. J. Physiol. Heart Circ. Physiol. **290**, H2098 (2006).
[57] M. E. Diaz, H. K. Graham, S. C. O'Neill *et al.*, Cell Calcium **38**, 391 (2005).
[58] T. R. Shannon, F. Wang, and D. M. Bers, Biophys. J. **89**, 4096 (2005).
[59] M. Kameyama, Y. Hirayama, H. Saitoh *et al.*, J. Electrocardiol. **36**, 125 (2003).
[60] E. G. Tolkacheva, D. G. Schaeffer, D. J. Gauthier *et al.*, Phys. Rev. E **67**, 031904 (2003).
[61] N. F. Otani and R. F. Gilmour, J. Theor. Biol. **187**, 409 (1997).
[62] M. A. Watanabe and M. L. Koller, Am. J. Physiol. Heart Circ. Physiol. **282**, H1534 (2002).
[63] D. R. Chialvo, D. C. Michaels, and J. Jalife, Circ. Res. **66**, 525 (1990).
[64] J. J. Fox, E. Bodenschatz, and R. F. Gilmour, Phys. Rev. Lett. **89**, 138101 (2002).
[65] A. Baher, Z. Qu, A. Hayatdavoudi *et al.*, Am. J. Physiol. Heart Circ. Physiol. **292**, H180 (2007).
[66] E. M. Cherry and F. H. Fenton, Am. J. Physiol. Heart Circ. Physiol. **286**, H2332 (2004).
[67] P. N. Jordan and D. J. Christini, Biophys. J. **90**, 672 (2006).
[68] M. E. Diaz, S. C. O'Neill, and D. A. Eisner, Circ. Res. **94**, 650 (2004).